Weierstraß-Institut
für Angewandte Analysis und Stochastik

Leibniz-Institut im Forschungsverbund Berlin e. V.

Preprint ISSN 2198-5855

Spatially modulated broad-area lasers for narrow lateral far-field divergence

Anissa Zeghuzi[1], Jan-Philipp Koester[1], Mindaugas Radziunas[2], Heike Christopher[1],

Hans Wenzel[1], Andrea Knigge[1]

submitted: July 15, 2021

[1] Ferdinand-Braun-Institut
Leibniz Institut für Höchstfrequenztechnik
Gustav-Kirchhoff-Straße 4
12489 Berlin
Germany
E-Mail: anissa.zeghuzi@fbh-berlin.de
jan-philipp.koester@fbh-berlin.de
hans.wenzel@fbh-berlin.de
heike.christopher@fbh-berlin.de
andrea.knigge@fbh-berlin.de

[2] Weierstrass Institute
Mohrenstr. 39
10117 Berlin
Germany
E-Mail: mindaugas.radziunas@wias-berlin.de

No. 2857
Berlin 2021

2020 *Mathematics Subject Classification.* 78A60, 78A45, 35Q60, 78-04, 37M05.

Key words and phrases. High-power broad-area semiconductor lasers, traveling-wave model, spatial modulation of gain and index, lateral modes, far-field narrowing.

This work was supported by the German Federal Ministry of Education and Research under contract 13N14026 as part of the EffiLAS/PLuS Project and partly by the Research Fab Microelectronics Germany (ref. 16FMD02).

Edited by
Weierstraß-Institut für Angewandte Analysis und Stochastik (WIAS)
Leibniz-Institut im Forschungsverbund Berlin e. V.
Mohrenstraße 39
10117 Berlin
Germany

Fax: +49 30 20372-303
E-Mail: preprint@wias-berlin.de
World Wide Web: http://www.wias-berlin.de/

Spatially modulated broad-area lasers for narrow lateral far-field divergence

Anissa Zeghuzi, Jan-Philipp Koester, Mindaugas Radziunas, Heike Christopher, Hans Wenzel, Andrea Knigge

Abstract

A novel laser design is presented that combines a longitudinal-lateral gain-loss modulation with an additional phase tailoring achieved by etching rectangular trenches. At 100 A pulsed operation, simulations predict a far-field profile with 0.3° full width at half maximum ($\Theta_{\mathrm{FWHM}} = 0.3^{\circ}$) where a 0.4°-wide main lobe contains 40% of the emitted optical output power ($\Theta_{40\%} = 0.4^{\circ}$). While far-field measurements of these structured lasers emitting 10 ns long pulses with 35 W peak power confirm a substantial enhancement of radiation within the central 1° angular range, the measured far-field intensity outside of the obtained central peak remains high.

1 Introduction

High-power broad-area lasers [10,24] provide the energy for a variety of laser systems and can also be applied for light detection and ranging (LiDAR) systems [2,11] used for autonomous driving and object detection. For the usage in LiDAR systems, wavelength stabilized lasers emitting short optical pulses with a high output power and good beam quality are needed [13]. However, due to the laterally broad emission aperture, broad-area lasers suffer from a deteriorated lateral beam quality [1,9]. To improve it, a variety of approaches have been proposed in the past, among them are coherently coupled laser arrays [5,7].

In laser arrays the broad lateral aperture is electrically separated into smaller injection stripes, that are alternated with interelement passive regions. In the same way, the real lateral refractive index distribution $n_0(x)$ is alternating with regions of high index n_{c} and regions of low index n_{l}, see Fig. 1(a). In array lasers two types of array modes are of importance, the index-guided modes, which have a real eigenvalue $\mathrm{Re}(\hat{n}_m)$ between n_{c} and n_{l}, and anti-index-guided modes, which have an eigenvalue below n_{l} [3]. Mode selection can be obtained by placing gain in the high index regions to excite index-guided modes as shown in Fig. 1 or by placing it in the low index regions to excite anti-index-guided modes (not shown here). Only the fundamental array mode of order 0 with the highest real eigenvalue $\mathrm{Re}(\hat{n}_m)$ shows a narrow lobe around 0° far-field angle, see Fig. 1(c), and hence it is the desired mode for laser operation. Because the field amplitude is co-phasal in each array element, the fundamental array mode is often refered to as in-phase mode, see Fig. 1(b), in contrast to the highest array mode (in this case of order 26) where the field amplitudes in adjacent elements have a π phase-shift and which is hence termed out-of-phase mode [3]. For the fabrication of most anti-index guided arrays a two-step epitaxy including regrowth is necessary [3], whereas index-guided arrays are easily fabricated. Stable fundamental mode operation has been reported in edge-emitting anti-index guided arrays [15,26], however it was never obtained in index-guided arrays [4] as overall coupling of array elements is difficult to achieve [4,14] and because the modal gain of the fundamental mode $\hat{g}_0$ is the lowest compared to all other array modes [6], see Fig. 1(d).

A mode selection mechanism that utilizes properties of near-field diffraction to obtain a low far-field divergence is the Talbot-type spatial filter [22]. The distance at which the diffraction pattern of a periodic near-field distribution with periodicity of Λ_x repeats itself is called the Talbot length z_T. Considering

DOI 10.20347/WIAS.PREPRINT.2857 Berlin 2021

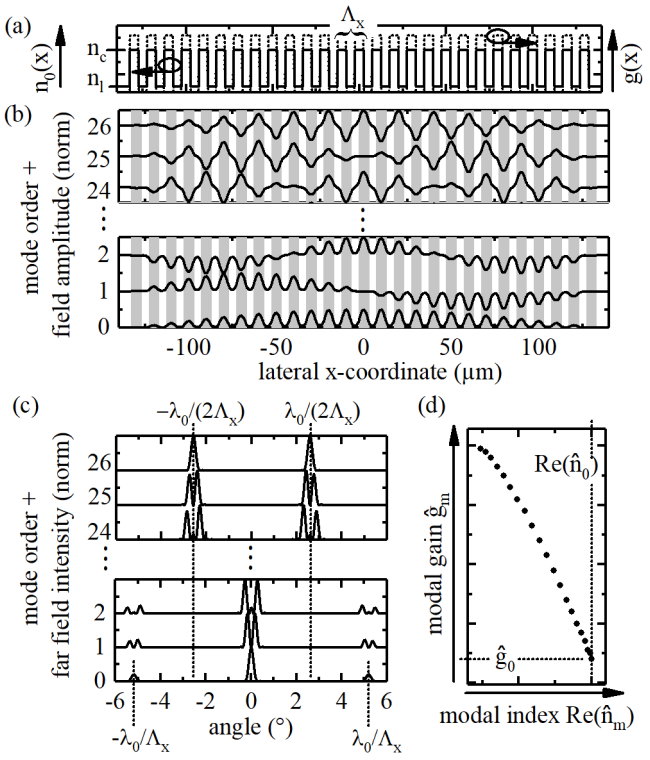

Figure 1: Modes of the index-guided array with lateral period $\Lambda_x = 10$ μm and total width of 270 μm. (a) Sketched distributions of real refractive index $n_0(x)$ and gain $g(x)$ under isothermal conditions and in the absence of spatial hole burning. (b) Field amplitudes of array modes. Grey shading: regions of high gain and refractive index. (c) Far-field intensities of the respective array modes displayed in (b). Only the fundamental array mode (in-phase mode) shows a narrow lobe around 0° far-field angle and small side lobes at $\pm\lambda_0/\Lambda_x$. The highest order mode (out-of-phase mode) has side lobes at $\pm\lambda_0/(2\Lambda_x)$. (d) Modal eigenvalues of the array modes, where the ordinate is the modal gain $\hat{g}_m = 2k_0\mathrm{Im}(\hat{n}_m)$ and the abscissa the real part of the modal index $\mathrm{Re}(\hat{n}_m)$.

paraxial propagation within a passive and homogeneous semiconductor material,

$$z_T = 2\Lambda_x^2 n_{\text{eff}}/\lambda_0 \equiv \Lambda_z, \tag{1}$$

where n_{eff} and λ_0 are the effective refractive index and the vacuum wavelength, respectively. At $z_T/2$ the near-field distribution of the in-phase mode repeats itself with a lateral shift of half its period.

This effect has already been used in early anti-guided laser arrays where free-running sections of length $z_T/2$ have been inserted between current injection stripes to facilitate the excitation of the in-phase mode [22]. In Ref. [21] it is shown that longitudinal-lateral gain-loss modulation with lateral Λ_x and longitudinal Λ_z periodicity of the contacted pads as sketched in 2(a), but without the additional modulation of the real refractive index, results in anisotropic gain. In these structures beam components propagating at angles to the propagation direction are attenuated, whereas the main lobe is amplified. These findings have already been employed theoretically with regards to amplifiers [18, 20] using the traveling-wave model approach described below. Until now, this concept could not be transferred to lasers. However, we show here that the in-phase mode can be successfully excited by additional phase tailoring, so that a very narrow central lobe far-field divergence close to the diffraction limit is predicted theoretically under pulsed operation. Parts of this work have been published in the dissertation of the first author [27].

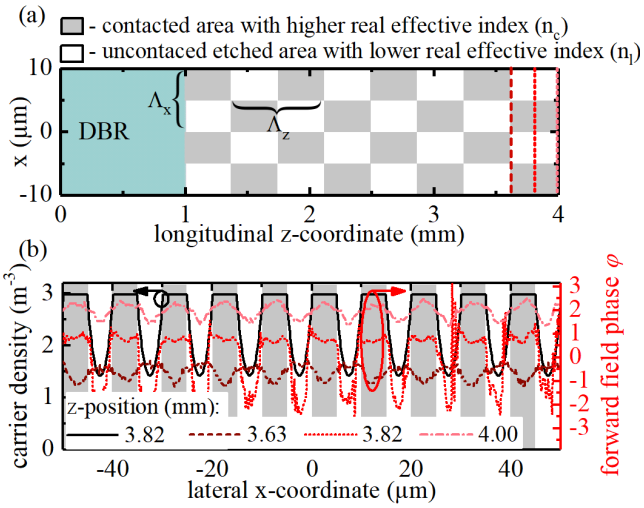

Figure 2: Operation principle of the presented spatially modulated DBR laser with lateral $\Lambda_x = 10\ \mu$m and longitudinal $\Lambda_z = 750\ \mu$m periodicity and additional phase tailoring. (a) Sketch of injection stripes. Vertical lines indicate the longitudinal z-positions of line plots in (b). (b) Exemplary lateral carrier density distribution (left axis - black) in the middle of the last longitudinal half-period ($z = 3.82$ mm) and forward field phase φ (right axis - red) at beginning ($z = 3.63$ mm), middle ($z = 3.82$ mm) and end ($z = 4$ mm) of this half-period.

2 Device structure and simulation model

The investigated lasers emit at a central wavelength of 905 nm and have a total cavity length of $L = 4$ mm including a DBR section of $L_{\text{DBR}} = 1$ mm, Fig. 2(a), and a total emission aperture width of $w_0 = 270\ \mu$m. The active region consists of a 12 nm thick single InGaAs quantum well and the cladding and optical-confinement layers are based on AlGaAs [13]. The front facet is low reflection coated to an intensity reflectivity of $R_L = 0.01$, whereas wavelength selective feedback at the rear facet is provided by the DBR grating. The devices are electrically driven with 10 ns long pulses at a repetition rate of 10 kHz so that heating between the pulses can be neglected. For details on the experimental set-up see Ref. [12].

The core of the dynamic simulation model utilized here is a 2(space)+1(time) dimensional traveling-wave model [19] defined in the (x, z)-plane, Fig. 2(a). The slowly varying complex amplitudes $u^{\pm}(x, z, t)$ obey the traveling-wave equations

$$\left[\frac{\partial_t}{v_{\text{g}}} \pm \partial_z + \frac{i}{2\bar{n}k_0}\partial_x^2 + ik_0\Delta n_{\text{eff}} + \mathcal{D}\right] u^{\pm} + ik_0\kappa^{\pm}u^{\mp} = f_{\text{sp}}^{\pm}, \tag{2}$$

which are coupled to a diffusive rate equation for the excess carrier density $N(x, z, t)$ in the plane of the active region,

$$\partial_t N = \partial_x \left[D_{\text{eff}}(N)\partial_x N\right] + \frac{j(x,z,t)}{ed} - R(N, \|u\|^2), \tag{3}$$

with $v_{\text{g}} = c/n_{\text{g}}$ and $k_0 = 2\pi/\lambda_0$. c, $n_{\text{g}} = 3.75$, $\lambda_0 = 905$ nm, $\bar{n} = 3.3$, e, $d = 12$ nm, and $\kappa(x, z)$ are the vacuum speed of light, the group refractive index, the center wavelength, a real valued reference index, the electron charge, the thickness of the active region (AR), and the counter-propagating field coupling coefficient, which is 2000 m^{-1} within the Bragg grating and is vanishing otherwise.

Both, the effective diffusion coefficient $D_{\text{eff}}(x, z, t) = D_{\text{eff}}(N, \partial_N\phi|_{y\in\text{AR}})$ and the injection current density $j(x, z, t) = -\sigma_p\partial_y\phi|_{y\in\text{AR}}$ are determined by the quasi-Fermi potential for the holes $\phi(x, y, z, t)$ within the p-doped layers of the diode (σ_p: hole conductivity). To find ϕ, for each z and

t, we solve the linear 2-D Laplace equation defined in the p-doped part of lateral-vertical (x-y) cross-sections of the diode. The (time-dependent) boundary conditions are determined by the applied voltage and the actual carrier density distribution. Simultaneous treatment of Eqs. (2), (3), and the above-discussed Laplace equation properly accounts for current spreading and spatial hole burning. In some of the presented simulations, seeking to suppress the impact of spatial hole burning, we assumed a single only 5 nm thick highly conducting ($\sigma_p = 10^5\,\Omega^{-1}\mathrm{m}^{-1}$) p-layer. For more details on the carrier spreading model, see Ref. [29].

The local photon density is defined as $\|u(x,z,t)\|^2 = |u^+|^2 + |u^-|^2$, whereas $R(x,z,t) = R(N,\|u\|^2) = AN + BN^2 + CN^3 + R_{\text{stim}}(N,\|u\|^2)$ is the recombination rate, where A, B, C are the Shockley-Read-Hall, spontaneous radiative and Auger recombination coefficients, and $R_{\text{stim}}(N,\|u\|^2)$ is the rate of stimulated recombination [19]. $f_{\text{sp}}^{\pm}(x,z,t)$ is the spontaneous emission contribution and the linear operator $\mathcal{D}$ is used to model dispersion of the optical gain [16].

The complex effective index deviation $\Delta n_{\text{eff}}(N,T,\|u\|^2)$ from the reference index $\bar{n}$ is given by

$$\Delta n_{\text{eff}}(x,z,t) = \Delta n_0 + \Delta n_N + \Delta n_T + i(g-\alpha)/(2k_0), \tag{4}$$

where $\Delta n_0(x,z)$, $\Delta n_N(x,z,t)$, and $\Delta n_T(x,z,t)$ account for a built-in, carrier density-dependent, and temperature-fluctuation-induced real-valued contributions to the refractive index change. The built-in index difference is produced by etching the uncontacted areas, so that Δn_0 is negative in these regions. $\Delta n_N(N)$ assumes the square-root-like dependence on the local carrier density.

The refractive index dependence on temperature, Δn_T, is derived for short pulse operation [30], i.e., assumes constant time-averaged temperature distribution, neglects heat flow but still accounts for short-time temperature fluctuations due to the rapidly varying heat sources.

Functions $g(x,z,t)$ and $\alpha(x,z,t)$ are contributions to the imaginary part of Δn_{eff} due to optical gain and absorption. Whereas the gain function $g(N,\|u\|^2)$ assumes the logarithmic dependence on the carrier density and accounts for the nonlinear gain saturation, the function α includes the free-carrier and two-photon absorption contributions [28].

Most of the parameters used in the presented simulations were taken from the literature [17, 23]. The carrier density dependency of the gain and refractive index as well as its dispersion were calculated using a microscopic gain model [25]. A comprehensive list of the used simulation parameters can be found on page 121 of Ref. [27]. Based on those parameters a good agreement between simulated and measured PI-characteristics of pulsed broad-area DBR lasers could be shown [27].

3 Novel spatially structured laser design

In lasers or amplifiers based on gain-loss material the current injection path is tailored by implantation of the uncontacted areas. In the lasers proposed here current-path tailoring is done by etching elongated rectangular trenches into the uncontacted areas, see Fig. 2(a). Within the etched areas the effective refractive index is lower, so that at the same time the phase of the propagating field beneath contacted and uncontacted regions, grey and white regions in Fig. 2 with the real effective refractive indices of n_{c} and n_{l}, respectively, gains a phase difference $\Delta\varphi$ which depends on the propagation distance Δz,

$$\Delta\varphi(\Delta z) = k_0 \Delta z \cdot \left[n_{\text{c}}(N,T,\Delta n_0) - n_{\text{l}}(N,T,\Delta n_0)\right]. \tag{5}$$

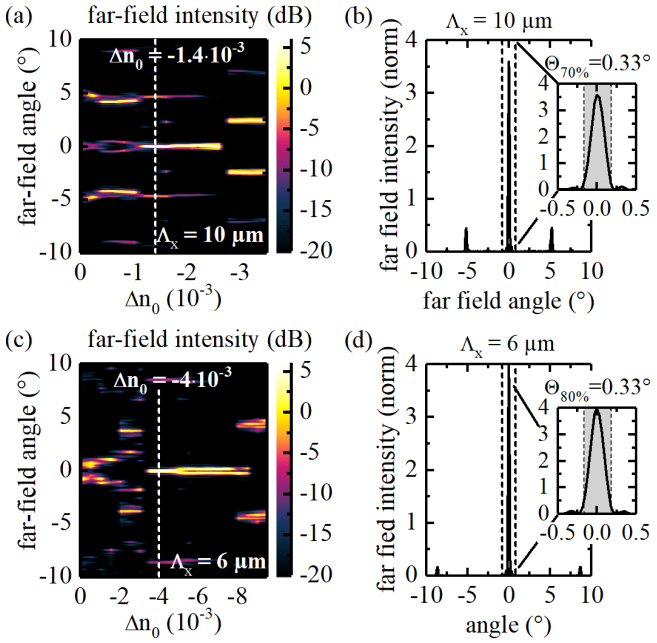

Figure 3: Far-field intensity distribution as function of the built-in index step Δn_0 within the uncontacted etched areas averaged over the last nanosecond of a 10 ns long pulse for a spatially modulated DBR laser with (a) $\Lambda_x = 10$ μm and $\Lambda_z = 750$ μm and (c) $\Lambda_x = 6$ μm and $\Lambda_z = 260$ μm. Far-field intensity distribution at the optimum built-in index step (b) $\Delta n_0 = -1.4 \cdot 10^{-3}$ for $\Lambda_x = 10$ μm and (d) $\Delta n_0 = -4 \cdot 10^{-3}$ for $\Lambda_x = 6$ μm. The laser is operated with 10 ns current pulses of approximately 100 A. A simplified model with negligible spatial hole burning and omitted temperature dependent changes of the refractive index was used.

To excite the in-phase mode a lateral phase-shift of $\Delta\varphi = \pm n\pi$, where n is an integer number, has to be introduced for the field propagating the distance $\Delta z = \Lambda_z/2$ starting at a period intersection. In this way the field's phase is tailored to self image with a lateral shift of half its lateral period after propagating through half a longitudinal period $\Lambda_z/2$, which is exemplarily illustrated in Fig. 2(b).

Generally n_c and n_i are not constant throughout the device and depend on the carrier density and fast temperature fluctuations [30] and therefore the optimum built-in index step varies along the longitudinal direction. To study the effect of phase tailoring and the impact of the longitudinal and lateral periodicity independent from these influences, in Fig. 3 simulation results for a simplified model are shown, derived under isothermal conditions and suppressed spatial hole burning.

The far-field intensity distribution is displayed here as function of the built-in index step Δn_0 within the uncontacted etched areas for two different spatially modulated laser designs at an injection current of approximately 100 A. In the upper case, Fig. 3(a) and (b), a lateral $\Lambda_x = 10$ μm and longitudinal $\Lambda_z = 750$ μm periodicity is chosen, whereas in the lower case, Fig. 3(c) and (d), the lateral and longitudinal periodicity is $\Lambda_x = 6$ μm and $\Lambda_z = 260$ μm, respectively, so that in both cases Eq. (1) is fulfilled.

In Figs. 3(a) and (c) it is clearly visible that by changing the built-index step Δn_0 the in-phase mode with a single lobed far field or the out-of phase mode, with side lobes at $\pm 2.6°$ in the upper case (a) or $\pm 4.3°$ in the lower case (c), can be selected. For the optimum built-in index step of $\Delta n_0 = -1.4 \cdot 10^{-3}$ for $(x, z) \in$ uncontacted etched areas and 0 elsewhere for $\Lambda_x = 10$ μm and $\Delta n_0 = -4 \cdot 10^{-3}$ for $(x, z) \in$ uncontacted etched areas and 0 elsewhere for $\Lambda_x = 6$ μm, the far-field intensity distribution is shown in Figs. 3(b) and (d), respectively. The percentage of power emitted within the full lateral

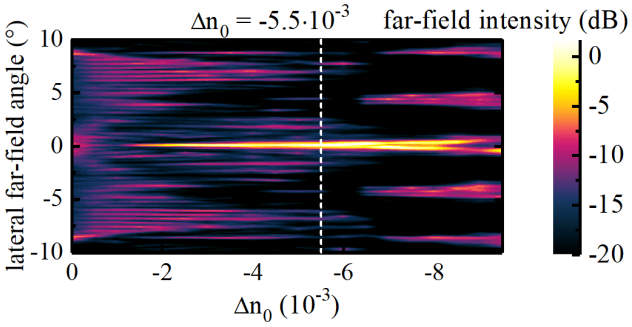

Figure 4: Same as Fig. 3(c) but using the full model including spatial hole burning and temperature dependent changes of the refractive index.

angle of $\Theta = 0.33°$ increases from 70% to 80% with increasing number of longitudinal periods from $N_z = 4$ to $N_z = 11.5$ and the side lobes are reduced. This indicates, that a high number of periods should be chosen to obtain the best performance.

Thus, for the smaller lateral periodicity of $\Lambda_x = 6$ μm the far-field intensity distribution as function of the built-in index step Δn_0 within the uncontacted etched areas is shown in Fig. 4 for the full model including spatial hole burning, current spreading and temperature induced refractive index changes. Including these effects the background intensity level of the far field is elevated compared to Fig. 3(c). Similarly to array lasers this is partly due to lateral spatial hole burning [8], because differences in the modal gain of the array supermodes are reduced. Furthermore, the uniformly etched pattern relies on longitudinal uniformity of the refractive index distribution and since n_c and n_i depend on the carrier density and fast temperature fluctuations, the phase shift $\Delta\varphi(\Lambda_z/2) \approx \pm n\pi$ for Eq. (5) between contacted and uncontacted elements is not obtained throughout the device and higher order modes are excited.

Furthermore the lowest far-field divergence is gained at a higher value of the built-in index step of $\Delta n_0 = -5.5 \cdot 10^{-3}$ compared to $\Delta n_0 = -4 \cdot 10^{-3}$ obtained for the simulations with suppressed spatial hole burning and without temperature induced index changes as shown in Fig. 3 (c). Now, the main lobe contains 40% instead of 80% of the emitted power leading to widths of $\Theta_{40\%} = 0.4°$ compared to $\Theta_{80\%} = 0.33°$, respectively, see blue dotted line in Fig. 5. This is due to the highly elevated carrier density and reduced refractive index at the edges of each contacted element and towards the rear facet as a result of longitudinal spatial hole burning. However, these values are still comparable to record values published for edge emitting antiguided array lasers, where a far-field angle containing 60% of the power of $\Theta_{60\%} = 0.62°$ for a 200 μm aperture was reported [26] for a pulsed peak output power of 10 W.

In Fig. 5 the measured (black solid) and simulated (blue dotted) far-field intensity distributions of the investigated laser are displayed at an injection current of approximately 100 A. In the simulation a very high output power of around 90 W is predicted, whereas the experimental pulse peak output power is $P_{\text{out}} = 35$ W. The origins of this discrepancy are not yet fully understood [28].

In the measured far-field intensity profile a strong central peak is observed, which is predicted by the simulation (blue dotted line), however, the intensity beside this central peak is significant. Still, the modulated laser design results in a substantial enhancement of radiation at very small far-field angles compared to the measured far-field profile of a conventional DBR broad-area laser of the same length, aperture and pulsed output power (red dashed - "reference"). Furthermore the full width at half maximum (FWHM) of the central lobe is only $\Theta_{\text{FWHM}} = 1°$ for the structured laser compared to $\Theta_{\text{FWHM}} = 14.9°$ for the conventional DBR broad-area laser, whereas the far-field angle containing

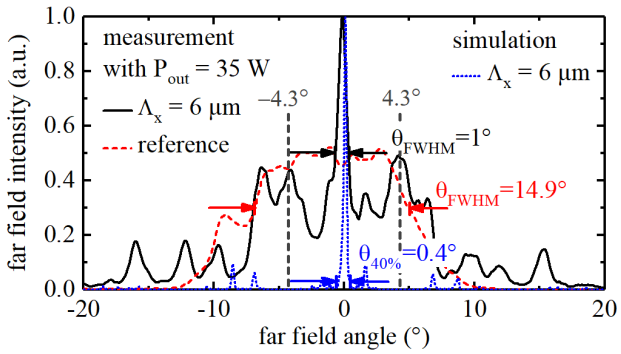

Figure 5: Comparison of the simulated (blue dotted) and measured (black solid) far-field intensity of a spatially modulated DBR laser with lateral $\Lambda_x = 6\ \mu$m, and longitudinal $\Lambda_z = 260\ \mu$m periodicity, and built-in index step $\Delta n_0 = -5.5 \cdot 10^{-3}$. The lasers are operated with 10 ns current pulses of approximately 100 A. For the measured laser a resulting output power of $P_{\text{out}} = 35$ W is achieved. Additionally the measured far-field intensity of a conventional unstructured DBR broad-area laser of the same length, aperture and output power is shown (red dashed - "reference").

95% of the power $\Theta_{95\%}$ is approximately twice as high. For both the structured as well as reference laser the pulsed peak output power is approximately 35 W, which is achieved for the structured lasers with a pulsed peak current of 100 A and for the conventional DBR broad-area laser at a lower pulsed peak current of 40 A due to the larger pumped region.

While the measurements indicate that this approach points in the right direction, optimum operation as indicated by the simulation results could not be reached. At $\Theta = \pm\lambda_0/(2\Lambda_x) = \pm 4.3°$ for example distinct peaks corresponding to the out-of-phase mode are visible, but also other peaks emerge that may correspond to other waveguide modes. The discrepancy may originate from an incorrectly predicted optimum built-in index step Δn_0, for example, when the total temperature or carrier density increase in high index regions, or the longitudinal variation of carrier density and temperature is higher than anticipated, so that the desired phase shift introduced between contacted and uncontacted areas is not realized throughout the resonator.

4 Conclusion

A novel laser design is presented that combines a longitudinal-lateral gain-loss modulation with an additional phase tailoring using etched rectangular trenches to excite the in-phase array supermode. A far-field profile with a FWHM of 0.3° which corresponds to an extremely narrow main lobe containing 40% of the emitted optical power within an angle of 0.4° is predicted theoretically at an injection current of 100 A under pulsed operation. While far-field measurements of the presented lasers emitting 10 ns long pulses with 35 W peak power confirm a substantial increase of intensity within the central angular range, the far-field intensity beside the obtained central peak remains significant.

References

[1] H. Adachihara, O. Hess, and E. Abraham. Spatiotemporal chaos in broad-area semiconductor lasers. *J. Opt. Soc. Am. B*, 10(4):658–665, 1993.

[2] B. Behroozpour, P.A.M. Sandborn, M.C. Wu, and B.E. Boser. Lidar system architectures and circuits. *IEEE Commun. Mag.*, 55(10):135–142, 2017.

[3] D. Botez. Monolithic phase-locked semiconductor laser arrays. In D. Botez and D.R. Scifres, editors, *High-Power Diode Lasers*, chapter 1, pages 1–72. Cambridge University Press, 1994.

[4] D. Botez and L.J. Mawst. Phase-locked laser arrays revisited. *IEEE Circuits and Devices Magazine*, 12(6):25–32, 1996.

[5] D. Botez and D.R. Scifres, editors. *Diode Laser Arrays*. Cambridge University Press, 1994.

[6] J.K. Butler, D.E. Ackley, and D. Botez. Coupled-mode analysis of phase-locked injection laser arrays. *Appl. Phys. Lett.*, 44:4, 1984. Erratum: vol. 44, p. 935, 1984.

[7] N.W. Carlsson. *Monolithic Diode-Layer Arrays (Springer Series in Electronics and Photonics 33)*. Springer-Verlag Berlin Heidelberg, 1994.

[8] Kuo-Liang Chen and Shyh Wang. Spatial hole burning problems in evanescently coupled semiconductor laser arrays. *Appl. Phys. Lett.*, 47(6):555–557, 1985.

[9] P. Crump, S. Böldicke, C.M. Schultz, H. Ekhteraei, H. Wenzel, and G. Erbert. Experimental and theoretical analysis of the dominant lateral waveguiding mechanism in 975 nm high power broad area diode lasers. *Semicond. Sci. Technol.*, 27:045001, 2012.

[10] R. Diehl, editor. *High-Power Diode Lasers: Fundamentals, Technology, Applications.* Springer, Berlin, Heidelberg, New York, 2000.

[11] C.-P. Hsu, B. Li, B. Solano-Rivas, A.R. Gohil, P.H. Chan, A.D. Moore, and V. Donzella. A review and perspective on optical phased array for automotive LiDAR. *IEEE J. Sel. Top. Quantum Electron.*, 27(1):1–16, 2021.

[12] A. Klehr, A. Liero, H. Wenzel, A. Zeghuzi, J. Fricke, R. Staske, and A. Knigge. Pico- and nanosecond investigations of the lateral nearfield of broad area lasers under pulsed high-current excitation. *Proc. SPIE*, 10553:105530K, 2018.

[13] A. Knigge, A. Klehr, H. Wenzel, A. Zeghuzi, J. Fricke, A. Maaßdorf, A. Liero, and G. Tränkle. Wavelength-stabilized high-pulse-power laser diodes for automotive LiDAR. *Phys. Status Solidi A*, 215(8):1700439, 2018.

[14] Ruoding Li and T. Erneux. Stability conditions for coupled lasers: series coupling versus parallel coupling. *Opt. Commun.*, 99(3):196–200, 1993.

[15] J.S. Major, D. Mehuys, and D.F. Welch. 11.5 W pulsed operation of antiguided laser diode array. *Electron. Lett.*, 28(12):1101, 1992.

[16] C.Z. Ning, R.A. Indik, and J.V. Moloney. Effective Bloch equations for semiconductor lasers and amplifiers. *IEEE J. Quantum Electron.*, 33(9):1543–1550, 1997.

[17] J. Piprek. *Semiconductor Optoelectronic Devices: Introduction to Physics and Simulation*. Elsevier, 2013.

[18] M. Radziunas, M. Botey, R. Herrero, and K. Staliunas. Intrinsic beam shaping mechanism in spatially modulated broad area semiconductor amplifiers. *Appl. Phys. Lett.*, 103(13):132101, 2013.

[19] M. Radziunas and R. Ciegis. Effective numerical algorithm for simulations of beam stabilization in broad area semiconductor lasers and amplifiers. *Math. Model. Anal.*, 19(5):627–646, 2014.

[20] M. Radziunas, R. Herrero, M. Botey, and K. Staliunas. Far-field narrowing in spatially modulated broad-area edge-emitting semiconductor amplifiers. *J. Opt. Soc. Am. B*, 32(5):993, 2015.

[21] K. Staliunas, R. Herrero, and R. Vilaseca. Subdiffraction and spatial filtering due to periodic spatial modulation of the gain-loss profile. *Phys. Rev. A*, 80(1):013821, 2009.

[22] P.D. Van Eijk. Analysis of the modal behavior of an antiguide diode laser array with Talbot filter. *J. Lightwave Technol.*, 9(5):629–634, 1991.

[23] I. Vurgaftman, J.R. Meyer, and L.R. Ram-Mohan. Band parameters for iii-v compound semiconductors and their alloys. *J. Appl. Phys.*, 89:5815–5875, 2001.

[24] H. Wenzel. Basic aspects of high-power semiconductor laser simulation. *IEEE J. Sel. Top. Quantum Electron.*, 19(5):1502913, 2013.

[25] H. Wenzel, G. Erbert, and P. Enders. Improved theory of the refractive-index change in quantum-well lasers. *IEEE J. Sel. Top. Quantum Electron.*, 5:637–642, 1999.

[26] H. Yang, L.J. Mawst, M. Nesnidal, J. Lopez, A. Bhattacharya, and D. Botez. 10 W near-diffraction-limited peak pulsed power from Al-free, 0.98 μm-emitting phase-locked antiguided arrays. *Electron. Lett.*, 33(2):136–137, 1997.

[27] A. Zeghuzi. *Analysis of spatio-temporal phenomena in high-brightness diode lasers using numerical simulations*. PhD thesis, Humboldt-Universität zu Berlin, Mathematisch-Naturwissenschaftliche Fakultät, 2020.

[28] A. Zeghuzi, M. Radziunas, H.-J. Wünsche, A. Klehr, H. Wenzel, and A. Knigge. Influence of nonlinear effects on the characteristics of pulsed high-power broad-area distributed Bragg reflector lasers. *Opt. Quantum Electron.*, 50(88):1–12, 2018.

[29] A. Zeghuzi, H. Wenzel, H.-J. Wünsche, M. Radziunas, U. Bandelow, and A. Knigge. Modeling of current spreading in high-power broad-area lasers and its impact on the lateral far field divergence. *Proc. SPIE*, 10526:105261H, 2018.

[30] A. Zeghuzi, H.-J. Wünsche, H. Wenzel, M. Radziunas, J. Fuhrmann, A. Klehr, U. Bandelow, and A. Knigge. Time-dependent simulation of thermal lensing in high-power broad-area semiconductor lasers. *IEEE J. Sel. Top. Quant.*, 25(6):1502310–1502310, 2019.